OPEN ACCESS



Polarization Substructure in the Spiral-dominated HH 111 Disk: Evidence for Grain Growth

Chin-Fei Lee¹, Zhi-Yun Li², Tao-Chung Ching³, Haifeng Yang⁴, Shih-Ping Lai⁵, Zhe-Yu Daniel Lin², and Ying-Chi Hu^{1,5}

Academia Sinica Institute of Astronomy and Astrophysics, No. 1, Sec. 4, Roosevelt Road, Taipei 106216, Taiwan, R.O.C.; cflee@asiaa.sinica.edu.tw

2 Astronomy Department, University of Virginia, Charlottesville, VA 22904, USA

3 National Radio Astronomy Observatory, P.O. Box O, Socorro, NM 87801, USA

4 Institute for Astronomy, School of Physics, Zhejiang University, Hangzhou, 310027 Zhejiang, People's Republic of China

5 Institute of Astronomy and Department of Physics, National Tsing Hua University, Hsinchu, Taiwan

Received 2024 July 4; revised 2024 July 21; accepted 2024 July 29; published 2024 August 8

Abstract

The HH 111 protostellar disk has recently been found to host a pair of spiral arms. Here we report the dust polarization results in the disk as well as the inner envelope around it, obtained with the Atacama Large Millimeter/submillimeter Array in continuum at $\lambda \sim 870 \,\mu \text{m}$ and $\sim 0.000 \,\text{m}$ resolution. In the inner envelope, polarization is detected with a polarization degree of \sim 6% and an orientation almost everywhere parallel to the minor axis of the disk and thus likely to be due to the dust grains magnetically aligned mainly by toroidal fields. In the disk, the polarization orientation is roughly azimuthal on the far side and becomes parallel to the minor axis on the near side, with a polarization gap in between on the far side near the central protostar. The disk polarization degree is $\sim 2\%$. The polarized intensity is higher on the near side than the far side, showing a near-far side asymmetry. More importantly, the polarized intensity and thus polarization degree are lower in the spiral arms but higher in between the arms, showing an anticorrelation of the polarized intensity with the spiral arms. Our modeling results indicate that this anticorrelation is useful for constraining the polarization mechanism and is consistent with the dust self-scattering by the grains that have grown to a size of $\sim 150 \,\mu m$. The interarms are sandwiched and illuminated by two brighter spiral arms and thus have higher polarized intensity. Our dust selfscattering model can also reproduce the observed polarization orientation parallel to the minor axis on the near side and the observed azimuthal polarization orientation at the two disk edges in the major axis. Further modeling work is needed to study how to reproduce the observed near-far side asymmetry in the polarized intensity and the observed azimuthal polarization orientation on the far side.

Unified Astronomy Thesaurus concepts: Star formation (1569); Stellar accretion disks (1579); Polarimetry (1278); Magnetic fields (994)

1. Introduction

With the powerful Atacama Large Millimeter/submillimeter Array (ALMA), dust polarization has been detected toward quite a few protostellar disks in millimeter and submillimeter wavelengths over the past decade (e.g., Kataoka et al. 2017; Stephens et al. 2017, 2023; Bacciotti et al. 2018; Cox et al. 2018; Girart et al. 2018; Harris et al. 2018; Hull et al. 2018; Lee et al. 2018, 2021; Dent et al. 2019; Sadavoy et al. 2019; Tang et al. 2023; Lin et al. 2024; Yang et al. 2024). It could be due to magnetically aligned grains (Andersson et al. 2015), dust selfscattering (Kataoka et al. 2015; Yang et al. 2016), or radiatively aligned grains (Kataoka et al. 2017; Tazaki et al. 2017), and more than one mechanism can be at work simultaneously, perplexing the analysis. If produced by magnetically aligned grains, it can be used to infer magnetic field morphology in the disks, which is crucial to studying the launching of the jets and winds from the disks (Konigl & Pudritz 2000; Shu et al. 2000) and disk accretion (Turner et al. 2014). If produced by dust self-scattering, it can be used to infer the grain size in the disks, allowing us to study whether there is a grain growth ultimately leading to planet formation.

Original content from this work may be used under the terms of the Creative Commons Attribution 4.0 licence. Any further distribution of this work must maintain attribution to the author(s) and the title of the work, journal citation and DOI.

In the protostellar disks, substructures, such as rings, gaps, and spirals, have also been detected and may help narrow down the dust polarization mechanism because they can affect dust polarization differently for different polarization mechanisms. In particular, the dust polarization due to dust self-scattering is affected by the asymmetry in the flux incoming from various directions, while the dust polarization due to the magnetically aligned grains is not. Recent dust polarization observations toward the well-studied HL Tau disk at a submillimeter wavelength of $870 \,\mu\text{m}$ have indeed shown that the rings and gaps in the disk have different polarization degrees and orientation, which can be attributed to both scattering and emission from the aligned grains (Stephens et al. 2023; Lin et al. 2024).

The HH 111 disk is a young ($\sim 5 \times 10^5 \, \rm yr$) Class I protostellar disk located in Orion at a distance of $\sim 400 \, \rm pc$ and has recently been found to harbor a pair of trailing spiral arms (Lee et al. 2020). Previous molecular line observations have found it to have a radius of $\sim 0.^{\prime\prime}4$ (160 au) and a Keplerian rotation (Lee et al. 2016). It drives the powerful collimated jet HH 111 (Reipurth et al. 1999), suggestive of a need for a poloidal magnetic field at the center of the disk according to the current popular jet launching models (Konigl & Pudritz 2000; Shu et al. 2000). The disk is close to edge-on, optimal for searching for a poloidal field in the disk. Dust polarization has been detected toward the disk at $\sim 0.^{\prime\prime}12$ resolution (Lee et al. 2018) at $\lambda \sim 870 \, \mu \rm m$ but showing a complex polarization pattern that

could be due to either magnetically aligned grains or dust self-scattering. In order to better determine the origin of the dust polarization, here we report the dust polarization detection at 2.4 times as high resolution as before and the modeling with the two polarization mechanisms. At this higher resolution, we can clarify the polarization pattern and its morphological relationship with the spiral arms. In addition, spiral arms have been argued to be excited by gravitational instability (GI) to facilitate disk accretion (Lee et al. 2020), allowing us to constrain the disk density and thus the dust absorption opacity in the disk. By modeling the better-resolved dust polarization, we can better determine the polarization mechanisms, searching for a poloidal field for jet launching and grain growth for planet formation.

2. Observations

Polarization observations toward the HH 111 system were carried out with ALMA in Band 7 in Cycle 3 (Project ID: 2015.1.00037.S) in 2016 and Cycle 5 (Project ID: 2017.1.00044S) in 2017. Since the details of the observations in Cycles 3 and 5 have been reported in Lee et al. (2018, 2020), respectively, we only recap the observation information most directly relevant to our investigation. In these observations, one pointing was used toward the center of the HH 111 system, with a field of view (the primary beam) having a size of \sim 17"8. The correlator was set up to have four continuum windows centered at 336.5, 338.5, 348.5, and 350.5 GHz for a total bandwidth of ~8 GHz centered at 343.5 GHz (corresponding to $\lambda \sim 870 \,\mu\text{m}$). The projected baseline lengths were \sim 14–8550 m after combining the observations in the two cycles. The maximum recoverable size scale was ~ 1.4 , enough to cover the disk seen in the continuum.

In both cycles, the uv data were calibrated with the Common Astronomy Software Applications package, with quasars J5010 +1800, J0552+0313, and J0522-3627 as bandpass, gain, and polarization calibrators, respectively. We also performed a phaseonly self-calibration to improve the map fidelity. The calibrated data from the two cycles were then combined into one set of calibrated data for mapping. In order to map the disk structure and dust polarization with increasing details, we used three decreasing robust factors for the uv weighting in making the maps. The robust factors are 2, 0.5, and 0. The resulting resolutions are 0.000×0.000 , 0.000×0.000 , and 0.000×0.000 , respectively. In the resulting Stokes I maps, the noise levels σ are $\sim 100 \,\mu\text{Jy beam}^{-1}$ (186 mK), $80 \,\mu\text{Jy beam}^{-1}$ (290 mK), and $50 \,\mu\text{Jy} \text{ beam}^{-1}$ (417 mK), respectively. In the resulting Stokes Q and U maps, the noise levels σ_p are $\sim 16 \,\mu\text{Jy beam}^{-1}$ (30 mK), 2 and 6 haps, the horse levels σ_p are 4.76 μ Jy beam (50 hrk), 18μ Jy beam (65 mK), and 26μ Jy beam (217 mK), respectively. The linear polarization intensity is defined as $P_i = \sqrt{Q^2 + U^2 - \sigma_p^2}$ and thus is bias-corrected. The fraction of the polarization is then defined as $P = P_i/I$. According to the ALMA Technical Handbook, the instrumental error on P is expected to be $\lesssim 0.2\%$ for the disk at the phase center, because the disk size is $\lesssim 1''$ and thus much smaller than one-third of the primary beam. Polarization orientations are defined by the E vectors.

3. Results

Figure 1 shows the maps of total intensity, polarized intensity, polarization orientation, and degree of continuum emission observed toward the center of the HH 111 protostellar system at $\lambda \sim 870~\mu m$. At this submillimeter wavelength, the continuum

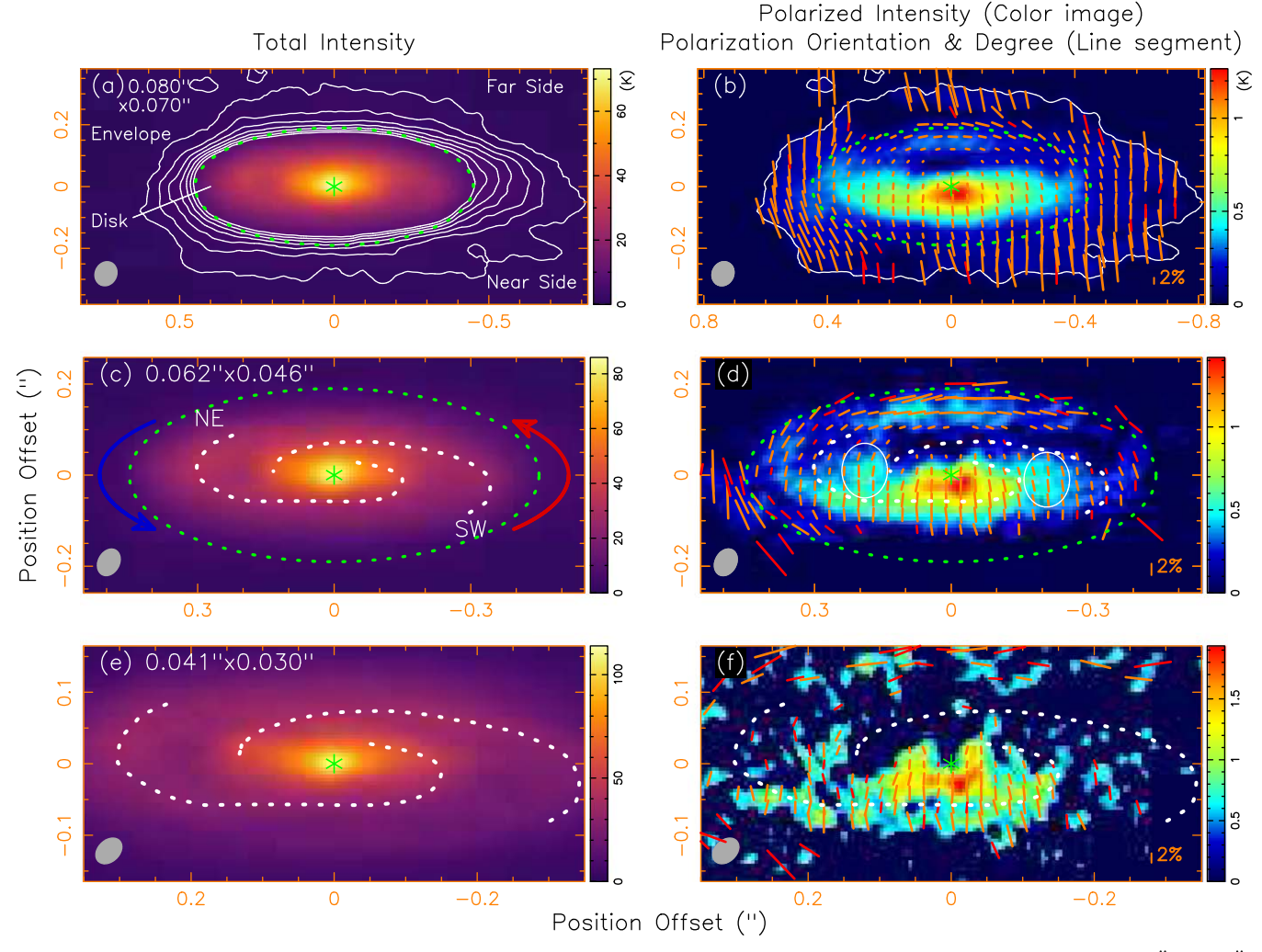
traces the dust emission in the disk and inner envelope (Lee et al. 2009). The maps have been rotated by 83° counterclockwise to align the disk major axis with the horizontal axis. They are presented from low (\sim 0."075 in Figures 1(a) and (b)) to medium (\sim 0."054 in Figures 1(c) and (d)) to high (\sim 0."035 in Figures 1(e) and (f)) angular resolution in order to reveal the disk structure and dust polarization with increasing detail.

At low angular resolution, the continuum emission is detected in both the disk and the inner part of the envelope around the disk (see Figure 1(a)). The contours of the continuum emission are crowded at a radius of ~ 0.45 on the major axis, indicating that the continuum emission intensity and thus the dust surface density increases rapidly there, confirming the formation of a disk within the envelope. The green dotted ellipse is thus added to mark the rough boundary between the disk and the envelope. It is highly elongated, consistent with the disk being tilted only $\sim 18^{\circ}$ away from being edge-on (Lee et al. 2020). As delineated by the contour at the lowest level (6σ detection), the inner envelope is not only detected around the two edges of the disk along the major axis but also above and below the disk extending slightly away from the disk. Interestingly, the polarization map (Figure 1(b)) shows a change in polarization morphology and a decrease in polarization degree from the envelope to the disk. In the envelope, the polarization orientation is almost everywhere parallel to the minor axis, while in the disk, the polarization orientation is azimuthal on the far side and then becomes parallel to the minor axis on the near side, with a polarization gap seen in between at ~ 0.007 above the central protostar. The polarization degree is \sim 6% in the envelope but decreases to \sim 2% in the disk. Inside the disk, the polarized intensity is higher on the near side than the far side, producing a near-far side asymmetric distribution in the polarized intensity. Near the central source, polarized emission is mainly detected on the near side.

Figure 1(c) zooms into the disk at medium angular resolution. The dotted curves delineate the northeastern (NE) and southwestern (SW) spiral arms previously identified at a slightly higher angular resolution of ~ 0.043 in Lee et al. (2020). The spiral arms are trailing, with their outer tips pointing in the direction opposite to the disk rotation measured before (as indicated by the blue and red curved arrows). At this resolution, it becomes clear that the polarized intensity is high at the two ends of the highly inclined disk, as well as the lower and upper rims of the disk (see Figure 1(d)). More importantly, the polarized intensity is lower and even below the detection in the spiral arms (as marked by the dotted curves) but higher in between the arms (as marked by the two white ellipses), except for the inner part of the NE spiral arm on the near side, where it is not resolved and thus not clear. This suggests an anticorrelation between the spiral arms and the polarized intensity (and thus the polarization degree). In order to check this behavior in the inner part of the NE spiral arm, we also present the total intensity and polarized intensity maps at high resolution in Figures 1(e) and (f), respectively. As can be seen, the polarized intensity there in the spiral arm could also be lower than its surroundings, and observations at higher resolution and sensitivity are needed to confirm it.

4. Origin of the Dust Polarization in the Inner Envelope

Dust polarization in the inner envelopes of young protostellar systems observed at $\lambda \sim 870~\mu m$ on a few hundred au



scale has been found to be mainly due to magnetically aligned grains (see, e.g., Cox et al. 2018; Maury et al. 2018; Kwon et al. 2019; Lee et al. 2019). For the case of HH 111, the dust polarization is also likely due to magnetically aligned grains. The inner envelope has a brightness temperature of $\sim 1-6$ K, much lower than the temperature there previously derived from the $C^{18}O$ gas, which is $\sim 40 \, \text{K}$ (Lee 2010). Therefore, the continuum emission is optically thin at the observed wavelength. As a result, the dust polarization is likely due to thermal emission of the dust, and the magnetic field orientation can be obtained by rotating the polarization orientation by 90°, as shown in Figure 2. In this case, the magnetic fields in the inner envelope are almost everywhere parallel to the major axis and are thus mainly toroidal, although a highly pinched poloidal (particularly radial) component is needed to explain the observed polarization orientations near the two edges along the major axis where the toroidal field component is close to the line of sight in this highly inclined system (and thus contributes little to the polarization). This is reasonable because the motion there is dominated by rotation (Lee et al. 2016), which twists the field lines into a predominantly toroidal

configuration (see, e.g., Machida et al. 2008; Li et al. 2013; Kwon et al. 2019).

5. Origin of the Dust Polarization in the Disk

Previous studies at a lower resolution of $\sim 0.0\%$ 12 suggested that the dust polarization in the HH 111 disk could be due to magnetically aligned grains, dust self-scattering, or both (Lee et al. 2018). In order to further determine the origin of the dust polarization in the disk, we construct a fiducial disk model and then generate dust polarization maps with these two polarization mechanisms to compare with the dust polarization mapped here at higher resolutions.

5.1. Disk Model

To construct the fiducial model, we adopt the same flared disk model previously used to model the continuum map of this disk obtained at a similar resolution in Lee et al. (2020). Therefore, the dust in the disk has the following mass density and temperature distributions in cylindrical coordinates (R, ϕ)

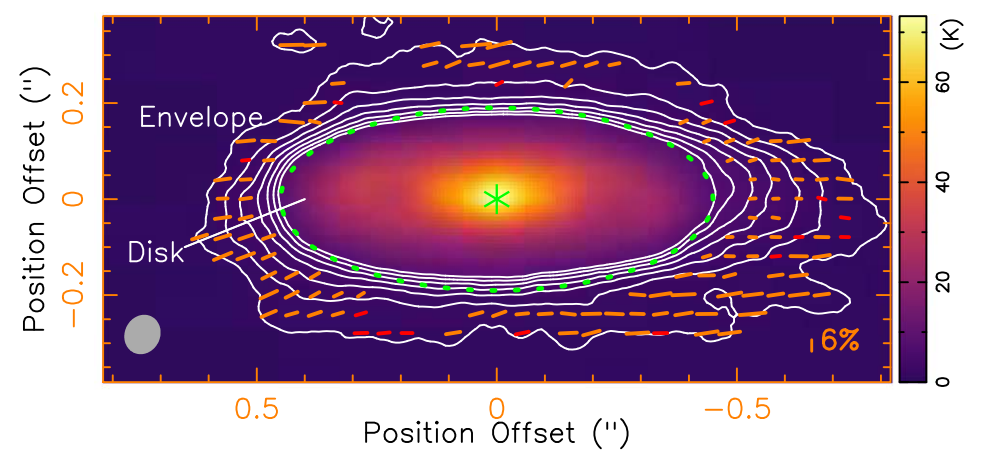


Figure 2. Magnetic field orientations in the inner envelope plotted on top of the total intensity of the continuum map. The color image, contour levels, and green dotted ellipse are the same as in Figure 1(a). The field orientations are obtained by rotating the polarization orientations by 90°.

z):

$$\rho(R, z) = \rho_{t} \left(\frac{R}{R_{t}}\right)^{-n} \exp\left(-\frac{z^{2}}{2h_{d}^{2}}\right),$$

$$T(R, z) = T_{t} \left(\frac{R}{R_{t}}\right)^{-q},$$
(1)

where $R_{\rm t}$ is the turnover radius to be defined below; $\rho_{\rm t}$ and $T_{\rm t}$ are the mass density and temperature in the disk midplane at $R_{\rm t}$, respectively; n and q are the power-law index for the density and temperature, respectively; and $h_{\rm d}$ is the pressure scale height. The scale height depends on the ratio of the sound speed to the angular rotation speed and thus increases with radius as $R^{(3-q)/2}$. It can decrease near the disk edge and is thus assumed to be given by

$$h_{\rm d}(R) = h_{\rm t} \begin{cases} \left(\frac{R}{R_{\rm t}}\right)^{(3-q)/2} & \text{if } R \leqslant R_{\rm t}, \\ \sqrt{1 - \frac{3}{4} \left(\frac{R - R_{\rm t}}{R_{\rm o} - R_{\rm t}}\right)^2} & \text{if } R_{\rm t} < R \leqslant R_{\rm o}, \end{cases}$$
(2)

so that it increases to $h_{\rm t}$ at $R_{\rm t}$ and then drops to $h_{\rm t}/2$ at the outer radius $R_{\rm o}$. Moreover, the disk is assumed to have a surface with a height $h_{\rm o} = \sqrt{2} \, h_{\rm d}$, where the density drops to 1/e of that in the midplane.

A pair of trailing spiral arms are also added into the disk. They are assumed to follow the logarithmic structure as excited by GI due to the self-gravity of the disk (Lee et al. 2020) with the following amplitude:

$$s = \cos\left[m\left(\phi - \frac{1}{a}\ln(R/R_s) - \phi_0\right)\right]. \tag{3}$$

Here m=2 is adopted to produce a pair of spiral arms, R_s is the outer radius of the spiral arms at $\phi = \phi_0$, and $\tan^{-1} a$ is the pitch angle. As seen in the HH 211 disk (Lee et al. 2023), the spiral arms are assumed to grow from the midplane. Therefore, the total dust density and temperature of the disk are assumed to decrease in the vertical direction from the midplane with the

following vertical profile:

$$\rho^{s}(R, \phi, z) = \rho_{t} \left(\frac{R}{R_{t}}\right)^{-n} \exp\left(-\frac{z^{2}}{2h_{d}^{2}}\right)$$

$$\times \left[1 + A(1+s)\exp\left(-\frac{z^{2}}{2h_{s}^{2}}\right)\right],$$

$$T^{s}(R, \phi, z) = T_{t} \left(\frac{R}{R_{t}}\right)^{-q} \left[1 + B(1+s)\exp\left(-\frac{z^{2}}{2h_{s}^{2}}\right)\right], \quad (4)$$

where h_s is the scale height of the spiral arms and is assumed to be a fraction of the disk scale height, i.e., $h_s = fh_d$ with f < 1. A and B are the spiral amplitude in density and temperature, respectively. The spiral arms are seen extending from a radius of \sim 0."4 down to \sim 0."1 from the central protostar (Lee et al. 2020). It is unclear how much closer they can extend because the disk structure there has not been resolved. Here they are assumed to extend further in with a small inner radius of 0."03, which is about a half of the beam size.

Additional physical quantities can be derived to constrain the model and check for consistency. Assuming that the disk also contains gas with a gas-to-dust mass ratio of \sim 100, the mean surface density (including gas and dust) of the disk at a given R can be derived by integrating the density over z and averaging it over ϕ :

$$\begin{split} &\Sigma(R) \sim 100 \int_{-h_o}^{h_o} \int_0^{2\pi} \rho^s(R, \phi, z) \frac{d\phi}{2\pi} dz \\ &= 100 \rho_t \left(\frac{R}{R_t}\right)^{-n} \sqrt{2\pi} h_d [\text{Erf}(1) + A K(f)] \\ &= \sum_t \left\{ \left(\frac{R}{R_t}\right)^{-p} & \text{if } R \leqslant R_t, \\ \left(\frac{R}{R_t}\right)^{-n} \sqrt{1 - \frac{3}{4} \left(\frac{R - R_t}{R_o - R_t}\right)^2} & \text{if } R_t < R \leqslant R_o, \end{cases} \end{split}$$

with the surface density power-law index $p \equiv n + (q - 3)/2$ and the mean surface density at R_t defined as

$$\begin{split} \Sigma_t &\equiv 100\sqrt{2\pi} \, \rho_t h_t [\text{Erf}(1) + A \, K(f)] \\ &\approx 21.6 \bigg(\frac{\rho_t}{3.6 \times 10^{-16} \, \text{g cm}^{-3}} \bigg) \\ &\times \bigg(\frac{h_t}{16 \, \text{au}} \bigg) [\text{Erf}(1) + A \, K(f)] \, \, \text{g cm}^{-2}, \end{split} \tag{6}$$

where Erf is the error function with $Erf(1) \approx 0.843$ and

$$K(f) \equiv \frac{\text{Erf}(\sqrt{1+1/f^2})}{\sqrt{1+1/f^2}} \approx f - \frac{f^3}{2}.$$
 (7)

Then, to check for GI, the Toomre Q parameter of the disk can be derived with (Toomre 1964)

$$Q(R) \approx \frac{c_s \Omega}{\pi G \Sigma(R)},$$
 (8)

where Ω is the angular rotation speed of the disk,

$$\Omega = \sqrt{\frac{GM(R)}{R^3}},\tag{9}$$

where M(R) is the total mass (including that of the central protostar and the disk) within R and c_s is the isothermal sound speed,

$$c_s = \sqrt{\frac{k\bar{T}(R)}{\mu m_H}},\tag{10}$$

where $\mu=2.33$ for molecular gas with H_2 and helium and $\bar{T}(R)$ is the mean temperature at a given R. Since the temperature decreases from the midplane to the surface, the mean temperature at a given R can be derived by averaging the density-weighted temperature over z as follows:

$$\bar{T}(R) = \frac{\int \int \rho^{s}(R, z) T^{s}(R, z) \frac{d\phi}{2\pi} dz}{\int \int \rho^{s}(R, \phi, z) \frac{d\phi}{2\pi} dz}$$

$$\approx T_{t} \left(\frac{R}{R_{t}}\right)^{-q} \frac{\operatorname{Erf}(1) + (A + B)K(f) + ABK(f/\sqrt{2})}{\operatorname{Erf}(1) + AK(f)}.$$
(11)

Thus, we have

$$Q(R) \approx \sqrt{\frac{\bar{T}(R)}{33 \text{ K}}} \frac{M(R)}{1.8 M_{\odot}} \left(\frac{160 \text{ au}}{R}\right)^{3} \left(\frac{21.6 \text{ g cm}^{-2}}{\Sigma(R)}\right).$$
 (12)

Hence, we can constrain the density parameter $\rho_{\rm t}$ assuming $Q\sim 1$ at $R_{\rm t}$.

The mass (including gas and dust) of the disk can be derived by integrating the mean surface density over R,

$$M_d \sim \int_0^{R_o} \Sigma(R) 2 \pi R dR = 2\pi C R_t^2 \Sigma_t$$

 $\approx 0.39 C \left(\frac{R_t}{160 \text{ au}}\right)^2 \left(\frac{\Sigma_t}{21.6 \text{ g cm}^{-2}}\right) M_{\odot},$ (13)

with

$$C \equiv \frac{1}{2-p} + \int_{1}^{x_0} x^{-n+1} \sqrt{1 - \frac{3}{4} \left(\frac{x-1}{x_0 - 1}\right)^2} dx, \tag{14}$$

where $x_0 \equiv \frac{R_o}{R_t}$. Estimation of the disk mass allows us to check if the disk is massive enough to be gravitationally unstable. Moreover, for a disk in vertical hydrostatic equilibrium, the scale height is expected to be

$$h_{\rm d}^e \sim \frac{c_s}{\Omega} \approx 17.3 \sqrt{\frac{\bar{T}(R)}{33\text{K}} \frac{1.8M_{\odot}}{M(R)} \left(\frac{R}{160 \text{ au}}\right)^3} \text{ au.}$$
 (15)

This expected scale height can also be checked against the bestfit value for consistency.

5.2. Fiducial Disk Model

The fiducial model with parameters appropriate for the HH 111 disk can be constructed by fitting the observed total intensity of the dust emission. For simplicity, we assume that the dust emission is purely thermal and the disk is everywhere in LTE. We use the radiative transfer code reported in Lee et al. (2021) to calculate the dust emission from the model and fit it (by eye) roughly to the observed maps.

A major uncertainty to calculate the dust emission in the model is the dust absorption opacity. Fortunately, since the disk is mostly optically thick, as found later, we can constrain the temperature in the disk with the observed brightness temperature. Then, since the spiral arms appear to be excited by GI (Lee et al. 2020), the Toomre Q parameters there are required to be \sim 1–2 (Durisen et al. 2007), allowing us to constrain the density of the disk and thus the dust absorption opacity to achieve the required optical depth (Beckwith et al. 1990; Lin et al. 2021). Moreover, this disk has also been mapped in ALMA Band 6 at $\lambda \sim 1.3$ mm (or 231 GHz) at ~ 0.11 f resolution (ALMA archive Project Code: 2016.1.00389.S) and Very Large Array (VLA) Band Ka at $\lambda \sim 9.1 \,\text{mm}$ (or 32.9 GHz) at ~ 0.007 resolution (Tobin et al. 2020; see Figure 3, first row). In Band 6, the disk emission was observed at a longer wavelength and thus should be less affected by dust self-scattering than that in Band 7. In Band Ka, although free-free emission is seen forming a collimated jet extending out from the inner disk, the emission in the outer disk should arise mainly from the thermal dust emission. As can be seen, the emission there also arises from around the spiral arms. With multiband observations, we can also define an opacity law $\kappa_{\lambda} = \kappa_0 (9.1 \text{ mm}/\lambda)^{\beta}$, where κ_0 is the dust opacity in Band Ka at $\lambda \sim 9.1$ mm and β is the dust opacity spectral index. Then, by fitting the multiband observations simultaneously, we not only can better constrain the model parameters in the disk but also can determine the parameters in the dust opacity law to constrain the grain properties.

For a geometrically thin accretion disk like the HH 111 disk, we have $q \sim 0.5$ –0.75 and $p \sim 1$ –1.5 (Armitage 2015). Thus, we have $n \sim 2.125$ –2.75. In order to simplify our fitting, we assume n=2.5. However, we allow the value of q to be obtained by fitting the distribution of the observed brightness temperature in the disk, which is mostly optically thick in Bands 6 and 7. Then, as shown in Figure 3, we find that a model with $R_{\rm t} \sim 0.^{\prime\prime}40$, $h_{\rm t} \sim 0.^{\prime\prime}04$, $R_{\rm o} \sim 0.^{\prime\prime}42$, $T_{\rm t} \sim 26$ K, $q \sim 0.65$, $\rho_{\rm t} \sim 3.6 \times 10^{-16}$ g cm⁻³, $a \sim -0.22$, $R_s \sim 0.^{\prime\prime}40$, $A \sim 0.5$, $B \sim 0.5$, $f \sim 0.4$, $\kappa_0 \sim 0.12$ cm⁻² g⁻¹, and $\beta \sim 1.4$

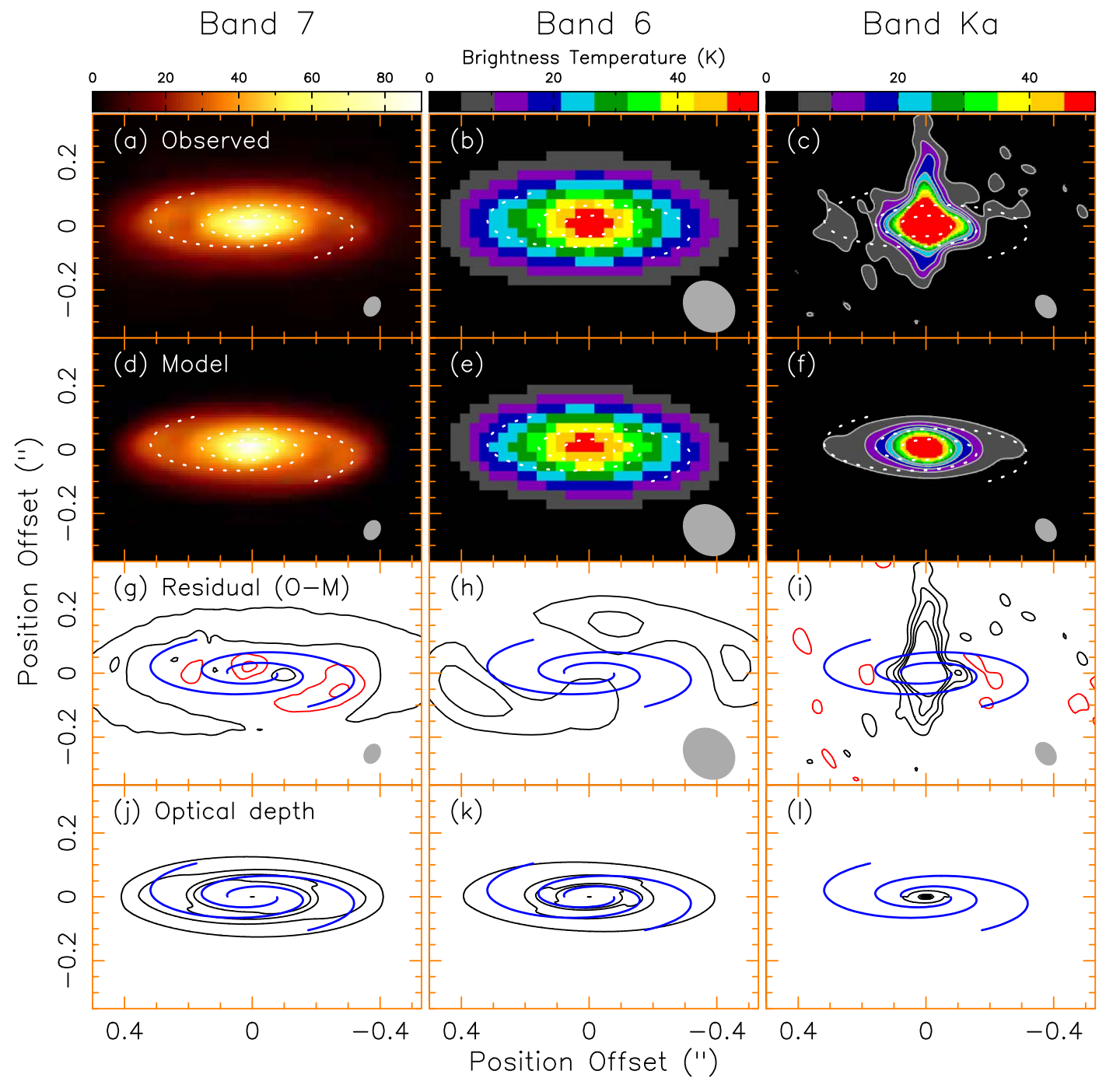


Figure 3. Observed maps (first row), model maps (second row), residual maps (third row, observed maps – model maps), and optical depth maps (fourth row) in Bands 7 (first column), 6 (second column), and Ka (third column). In (g)–(i), black contours are for positive residuals and red contours for negative residuals. In (g), contours start at 10σ with a step of 7σ , where $\sigma = 290$ mK. In (h), contours start at 20σ with a step of 10σ , where $\sigma = 110$ mK. In (i), contours start at 2.5σ with a step of 2.5σ , where $\sigma = 2.0$ K. Optical depth starts from 1 with a step of 2.

can roughly reproduce the observed disk emission in Bands 6 and 7 and the spiral structures in Bands 7 and Ka, except for the inner disk and jet in Band Ka. Figures 4(a) and (b) show the resulting density and temperature distributions of the disk, produced by the visualization application ParaView using volume rendering (Ahrens et al. 2005). Note that with the selected temperature range, we can see through the disk to the spiral arms in the disk midplane. However, with the selected density range, we can only see the overall density structure of the disk and cannot clearly see the spiral arms because the density contrast between the spiral arms and interarms is much

smaller than the density range in the disk. In Bands 6 and 7, the faint residual emission seen around the disk arises from the inner envelope around the disk and thus cannot be reproduced from our model that only includes the disk. Note that the spiral parameters a and R_s are in good agreement with those previously reported in Lee et al. (2020). The value of ρ_t is set to have a Toomre Q parameter of ~ 1 at R_t , so that the resulting Toomre Q parameter is $\sim 1-2$ for most of the disk from $R \sim 0.11$ to R_o , as required for the disk being gravitationally unstable. The resulting κ_λ values are 3.2, 1.8, and 0.12 cm² g⁻¹ of dust at $\lambda = 0.87$, 1.3, and 9.1 mm,

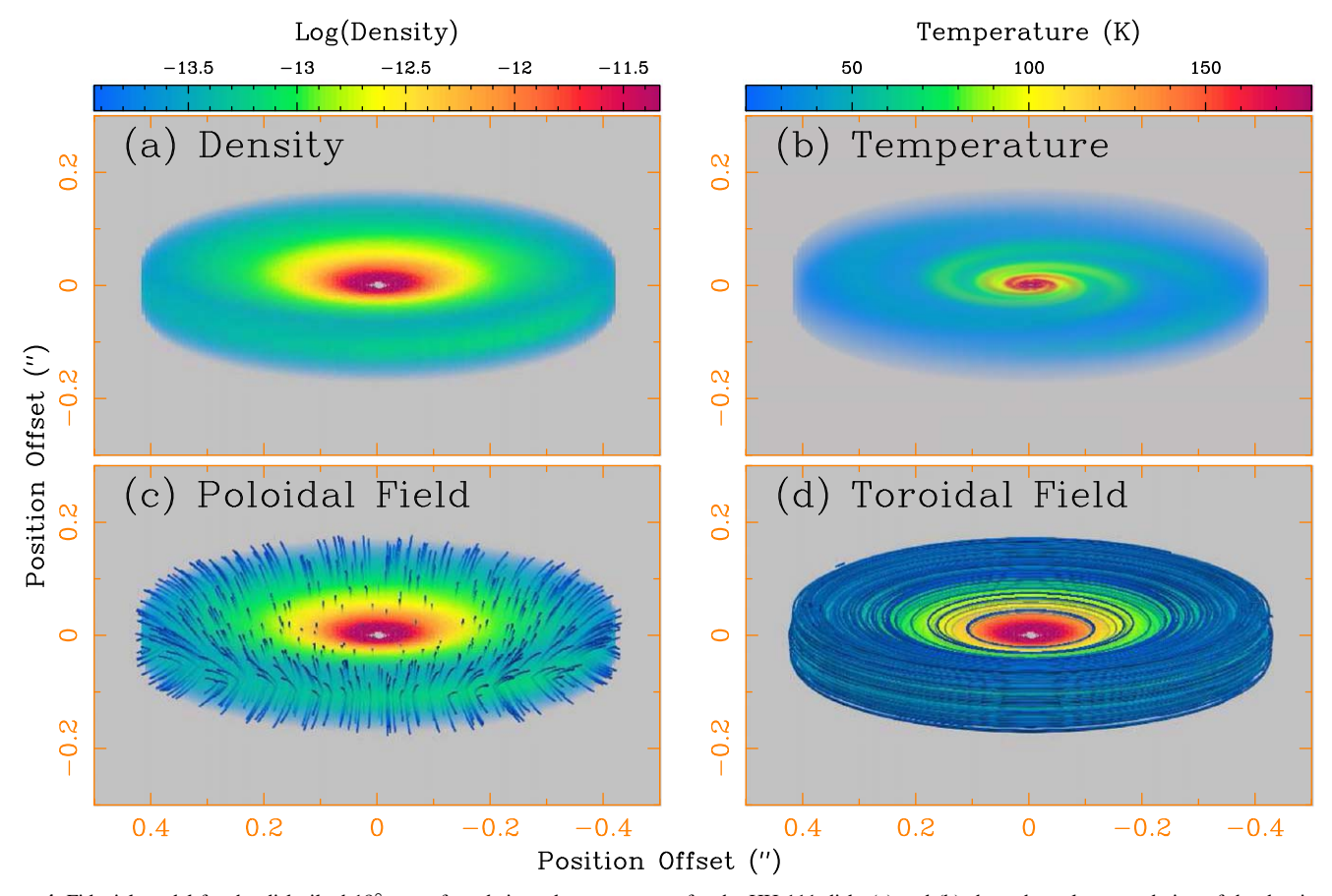


Figure 4. Fiducial model for the disk tilted 18° away from being edge-on, as seen for the HH 111 disk. (a) and (b) show the volume rendering of the density and temperature distributions in the model, respectively. See text for the explanation. (c) Highly pinched poloidal fields added to the disk. (d) Toroidal fields added to the disk.

respectively. In addition, the value of κ_{λ} at $\lambda = 0.87$ mm is similar to those adopted in the Class 0 disks; e.g., in HH 211 (Lee et al. 2023) and HH 212 (Lee et al. 2021; Lin et al. 2021), the value of κ_{λ} at $\lambda = 1.3$ mm is similar to those adopted in the Class 0/I disks, e.g., L1527 (van't Hoff et al. 2023) and R CrA IRs7Ba (Takakuwa et al. 2024), and the value of κ_{λ} at $\lambda = 9.1$ mm is similar to those adopted in the Class 0/I disks (Tobin et al. 2020). The resulting mean dust surface density $\Sigma_t/100$ is ~ 0.22 g cm⁻² at R_t , and thus the dust emission of the disk is mostly optically thick in Bands 6 and 7 and mostly optically thin in Band Ka. The resulting disk mass M_d is $\sim 0.58 M_{\odot}$. Since the protostar and disk were previously found to have a total mass of $\sim 1.8~M_{\odot}$ (Lee et al. 2016), the protostar has a mass of $\sim 1.22 \, M_{\odot}$. Therefore, the disk-to-protostar mass ratio is \sim 0.48, and thus the disk is massive enough to excite GI for two prominent spiral arms (see, e.g., Dong et al. 2015). The expected scale height in vertical hydrostatic equilibrium is $h_t^e \sim 17.3$ au, similar to the best-fit value of h_t , suggesting that the disk is in vertical hydrostatic equilibrium. The scale-height-to-radius ratio at R_t is ~ 0.1 , indicating that the disk is geometrically thin and much thinner than the younger disks in, e.g., HH 212 (Lee et al. 2021) and HH 211 (Lee et al. 2023). In summary, the obtained model parameters are reasonable; thus, the model can be considered as a fiducial model for our study of dust polarization.

5.3. Magnetically Aligned Grains

Given the fiducial disk model, we explore if the dust polarization in the disk in Band 7 can be due to magnetically aligned grains. Since this polarization mechanism only slightly affects the emission intensity by about the polarization fraction, which is $\sim\!2\%$, no adjustment of the model parameters is needed. We use the radiative transfer code reported in Lee et al. (2021), in which dust polarization by magnetically aligned grains is included with a parameter α defining the maximum fraction of polarization in an optically thin region. Here $\alpha=0.1$ is used to produce the small polarization degree of $\sim\!2\%$ as observed in the disk, which is optically thick in Band 7 and thus expected to have a polarization fraction significantly reduced from the maximum value. Interestingly, a similar α value has been adopted to reproduce the polarization images of HL Tau observed from ALMA Band 7 (Stephens et al. 2023) to the VLA Q band (Lin et al. 2024).

It is believed that magnetically aligned grains have their long axis perpendicular to the field lines (Andersson et al. 2015). Therefore, the dust polarization orientation is perpendicular to the magnetic field in the optically thin region. In the optically thick region, the polarization fraction drops to zero for an isothermal line of sight. However, if there exists a temperature gradient, then the polarization orientation can be perpendicular to the magnetic field if the temperature increases to the observer or parallel to the magnetic field if the temperature decreases to the observer (Yang et al. 2017; Lin et al. 2020). The polarized intensity drops to zero during the transition from the optically thick to more optically thin region, producing a polarization gap near $\tau \sim 4$ (see, e.g., Lee et al. 2021). At face value in the optically thin limit (see Figure 3(j)), the observed

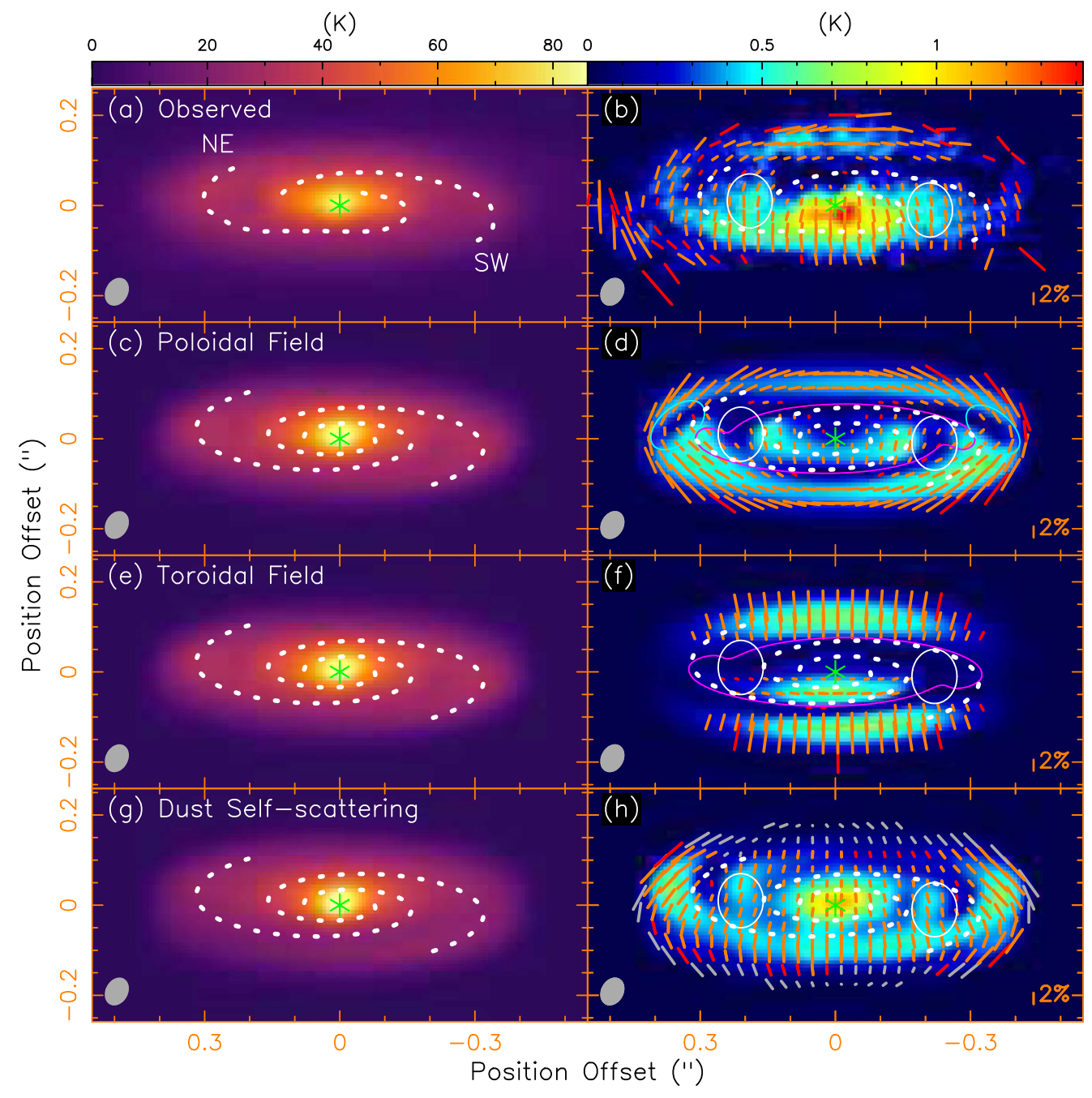


Figure 5. Comparison of the polarization between the observed maps (first row) and the model maps derived from the magnetically aligned grains by poloidal fields (second row) and toroidal fields (third row) and the model map due to dust self-scattering (fourth row). In the right column, the white ellipses mark the interarm regions. In (d), the cyan ellipses mark the regions where the polarization gaps are due to depolarization of mutually orthogonal polarization. In (h), gray line segments are added to show the detections below 3σ .

azimuthal polarization pattern on the far side (Figure 1(d)) could be due to poloidal fields that are highly pinched toward the equatorial plane (see Figure 4(c)), while the observed polarization orientation parallel to the minor axis on the near side could be due to toroidal fields (see Figure 4(d)).

In the following, we present the polarization results of the model for the two field morphologies separately in order to check these possibilities. Figures 5(c) and (d) show, respectively, the resulting intensity map and polarization map when the disk is threaded with highly pinched poloidal fields. Notice that dashed curves are added to guide the reader for the spiral arms. In this case, the region with $\tau \sim 4$ (marked by the

magenta contour in Figure 5(d)) happens to be along the outer part of the spiral arms, producing clear polarization gaps there. The gap along the SW arm on the far side is observed, but observations at higher resolution are needed to check if the gap along the NE arm on the near side is also observed. Outside the polarization gaps at $\tau \sim 4$, the polarization orientation is roughly azimuthal, as expected, and the polarization gaps at the two disk edges (marked by two tilted cyan ellipses) are due to the depolarization of mutually orthogonal polarization along the sight lines toward these regions. This azimuthal orientation is also observed on the far side of the disk but not on the near side of the disk, where the observed orientation is parallel to the

minor axis. Interior to the polarization gaps at $\tau \sim 4$, the polarization orientations are roughly parallel to the minor axis (which is expected because of polarization reversal due to dichroic absorption along optically thick sight lines where the temperature decreases to the observer) and pointing slightly toward the minor axis when moving away from the major axis. Although the observed polarization orientations are also roughly parallel to the minor axis, they point slightly outward from the minor axis. In the model, close to the central source, polarized emission is mainly produced on the near side. Similar behavior is also seen in the observation, although with much higher intensity. More importantly, excluding the polarization gaps along the spiral arms produced by $\tau \sim 4$ and the polarization gaps due to the depolarization of mutually orthogonal polarization, this model produces polarization gaps (regions marked by the white ellipses) in between the spiral arms and high polarization along the spiral arms and is thus opposite to the observation.

Figures 5(e) and (f) show, respectively, the resulting intensity map and polarization map when the disk is threaded with toroidal fields. As in the case of poloidal fields, polarization gaps are clearly seen along the spiral arms where $\tau \sim 4$. Outside these gaps, the polarization orientations are mainly parallel to the minor axis and pointing slightly away from the minor axis when moving away from the major axis and thus more likely pointing radially outward as expected. This is different from the observed polarization orientations, which are almost exactly parallel to the minor axis on the near side and azimuthal on the far side. Interior to the polarization gaps at $\tau \sim 4$, the polarization orientations are perpendicular to the minor axis, also different from the observed, which are almost parallel to the minor axis.

In summary, it is unclear if the observed dust polarization of the disk can be due to magnetic alignment of the dust grains. The model with poloidal fields can account only for the azimuthal polarization orientations on the far side, while the model with toroidal fields fails to account for most polarization orientations, including those polarization orientations parallel to the minor axis on the near side. Adding the toroidal fields into the model with poloidal fields will tilt the polarization orientations to one side (not shown), also inconsistent with the observed polarization orientations.

5.4. Dust Self-Scattering

At our observed wavelength of \sim 870 μ m, dust scattering is efficient when the maximum grain size $a_{\rm max} \sim 70$ –210 μ m (with a peak at \sim 140 μ m) and becomes inefficient when a_{max} increases to $\gtrsim 300 \,\mu\text{m}$ (Kataoka et al. 2015). Recently, DSHARP dust opacities have been used to model the dust emission in protoplanetary disks (Birnstiel et al. 2018), assuming compact grains with a MRN size distribution. For this type of grain with $a_{\rm max} \sim 70-210 \,\mu{\rm m}, \ \kappa_{\lambda}$ is $\sim 0.8-$ 1.9 cm² g⁻¹ of dust, much smaller than that required in our fiducial model. We could reduce κ_{λ} in the fiducial model by increasing the density and thus the disk mass. However, since the disk mass to protostellar mass ratio is already large in our model, it is not clear if the disk mass can be increased significantly, unless the total mass of the protostar and disk is found to be higher. It is possible that the dust grains in this disk have a different composition from that assumed in DSHARP for older disks where the planet formation has begun. Here, for demonstration purposes, we adopt the DSHARP grains with

 $a_{\rm max}$ of 170 μ m, which has a not-too-small absorption opacity and is still efficient in dust scattering. The dust absorption opacity is $\sim 1.4~{\rm cm}^2~{\rm g}^{-1}$ of dust but is scaled up to $3.2~{\rm cm}^2~{\rm g}^{-1}$ of dust. The scattering opacity is $\sim 10~{\rm cm}^2~{\rm g}^{-1}$ of dust, giving rise to an albedo of ~ 0.76 . Note that this combination could be obtained if using porous grains (Tazaki et al. 2019).

We use RADMC-3D (Dullemond et al. 2012) to calculate the dust polarization due to dust self-scattering. Since the dust scattering causes an additional extinction to the disk emission, the disk temperature is increased by a factor of ~ 1.3 in order to roughly match the observed brightness temperature in the disk, as shown in Figure 5(g). Figure 5(h) shows the polarized intensity, orientation, and degree generated from the model. The polarization degree is \sim 2%, roughly consistent with the observation. The polarization orientation is mainly parallel to the minor axis pointing slightly away from the minor axis and becomes azimuthal at the two disk edges in the major axis, as seen in the self-scattering model presented in Yang et al. (2017) when the disk is optically thick. The model produces bright polarized emission at the lower disk rim and the two disk edges, as seen in the observation, due to a sharp decrease of the disk density there in our model, creating an asymmetry in the flux toward the lower rim and two edges. However, the model produces very faint polarized emission at the upper rim, inconsistent with the observation in which bright polarized emission is detected with azimuthal orientation. Adding the line segments (gray) for polarized intensity at lower levels, we can see that polarization orientations in the upper rim (where the emission is optically thin) are also quite different from being azimuthal.

More importantly, we find that the polarized intensity is lower along the spiral arms but higher in the interarms (as marked by the two white ellipses) between the spiral arms. This behavior is better seen along the major axis, because the incident light along the major axis is scattered by 90° into the line of sight and is thus maximally polarized (Yang et al. 2017). This distribution is also seen in the observed polarization map. The detailed distribution and intensity of the polarized emission are different from the observed polarization map because the actual spirals may have different physical properties (e.g., temperature and density) from those used in our simple model, and the actual dust grains are different from the DSHARP grains. The interarms are sandwiched and illuminated by two brighter spiral arms and thus have higher polarized intensity. Going inward to around the central source, no clear near-far side asymmetry is seen in the polarized intensity, inconsistent with the observed. Such a near-far side asymmetry can be produced with a geometrically thick disk viewed at a moderate inclination angle (Yang et al. 2017). However, since the disk in our model is highly inclined, no clear near-far asymmetry can be seen, even if we increase the scale height h_t by 30% (the uncertainty in our model) to have a geometrically thick disk.

In summary, the dust self-scattering model can roughly reproduce most of the observed polarization features, including the polarization orientations parallel to the minor axis on the near side, the azimuthal polarization orientations near the disk edges, and the anticorrelation of the polarized intensity with the spiral arms (i.e., higher polarized intensity in between the spiral arms and lower polarized intensity along the spiral arms). Therefore, the observed dust polarization in the HH 111 disk is likely dominated by dust self-scattering, with possible contributions from other mechanisms, such as grains aligned

by a poloidal magnetic field. The polarization orientations parallel to the minor axis and the azimuthal polarization orientations near the disk edges have also been seen in other disks and attributed to the dust self-scattering (e.g., Bacciotti et al. 2018; Girart et al. 2018). Thus, our result indicates a grain growth in the disk to a size of $\sim 150~\mu m$. The best-fit dust opacity spectral index $\beta \sim 1.4$ also supports this grain growth possibility.

The anticorrelation of the polarized intensity with the spiral arms is reminiscent of that seen in HL Tau (Stephens et al. 2023), where the rings are observed to be less polarized than the gaps. The interpretation for the HL Tau case was that the polarizations in the rings and gaps are both produced by azimuthally aligned, effectively prolate grains through both thermal emission and scattering. The lower optical depth in the gaps allows the thermal emission of the aligned grains (which has a much higher intrinsic polarization fraction) to dominate over scattering, producing a relatively high polarization fraction. The higher optical depth in the rings reduces the thermal polarization through dichroic extinction to such an extent that it becomes dominated by scattering, which tends to produce a relatively low polarization fraction. It is plausible that the polarization observed in our case of HH 111 is also produced by scattering aligned grains. In particular, azimuthally aligned effectively prolate grains would readily produce the azimuthal pattern observed in the upper (far) side of the outer disk outside the SW spiral through thermal emission if the optical depth there is relatively low, such that thermal emission by aligned grains can dominate scattering as well as part of the polarization parallel to the minor axis observed in the lower (near) side of the inner disk from polarization reversal due to dichroic extinction if the optical depth there is large enough (see Figure 5(d); see also Figure 9 in Lin et al. 2020). In the lower (near) side of the disk, scattering could be enhanced compared to that in the far side if the disk is geometrically thick enough for the $\tau = 1$ surface on the near side to become significantly more inclined to the line of sight than that on the far side (Yang et al. 2017). With a potential boost from this geometric effect, scattering could dominate over polarized thermal emission over most of the disk (except near the edge on the far side) and broadly explain the main observed features, particularly the weaker polarization observed in the spiral arms, as we have demonstrated through detailed modeling (see Figure 5(h)). In this scenario, the main difference between HH 111 and HL Tau is that the former is more inclined and has a geometrically thicker dust layer responsible for the polarized submillimeter emission, which increases the scattering-induced polarization on the near side relative to that on the far side, and a larger optical depth along the line of sight (boosted by a more edge-on disk inclination), which further enhances the minoraxis-aligned polarization on the near side of the disk by flipping the orientation of the polarization emitted by the azimuthally aligned effectively prolate grains by 90° through dichroic extinction. The flipping is more likely on the near side of the disk than the far side because, for highly inclined disks such as HH 111, the polarized thermal emission from aligned grains near the midplane passes through a larger column of dust (and gas) along the line of sight on the near side than the far side (as illustrated by the cartoon in Figure 11 of Takakuwa et al. 2024); the flipped polarization adds to (rather than cancels) the polarization from scattering at locations along the minor axis. Another potential difference is that the scattering

(nonspherical) grains in the HH 111 disk could be aligned by a (pinched) poloidal field, which can broadly explain the azimuthal polarization pattern (of nonscattering origin) observed near the disk edge on the far side (see Figure 5(d)). Detailed calculations that include self-consistent treatment of both thermal emission and scattering by aligned grains, particularly optical depth effects such as dichroic extinction (which may be different on the near and far sides of the disk), are needed to test the scenario quantitatively. Similar to the work on HL Tau, additional observations at longer wavelengths can further distinguish the origin of polarization. Since polarization from scattering decreases at longer wavelengths and that from aligned grains increases, longer-wavelength observations can better reveal the underlying grain alignment configuration.

Acknowledgments

We thank the anonymous referee for useful comments. This Letter makes use of the following ALMA data: ADS/JAO. ALMA# 2015.1.00037.S and 2017.1.00044.S. ALMA is a partnership of ESO (representing its member states), NSF (USA) and NINS (Japan), together with NRC (Canada), NSTC and ASIAA (Taiwan), and KASI (Republic of Korea), in cooperation with the Republic of Chile. The Joint ALMA Observatory is operated by ESO, AUI/NRAO and NAOJ. C.-F.L. and Y.-C.H. acknowledge grants from the National Science and Technology Council of Taiwan (110-2112-M-001-021-MY3 and 112-2112-M-001-039-MY3) and the Academia Sinica (Investigator Award AS-IA-108-M01). Z.Y.L. is supported in part by NASA 80NSSC20K0533 and NSF AST-2307199.

ORCID iDs

Chin-Fei Lee https://orcid.org/0000-0002-3024-5864
Zhi-Yun Li https://orcid.org/0000-0002-7402-6487
Tao-Chung Ching https://orcid.org/0000-0001-8516-2532
Haifeng Yang https://orcid.org/0000-0002-8537-6669
Shih-Ping Lai https://orcid.org/0000-0001-5522-486X
Zhe-Yu Daniel Lin https://orcid.org/0000-0001-7233-4171

References

```
Ahrens, J., Geveci, B., & Charles, L. 2005, ParaView: An End-User Tool for
  Large Data Visualization (Amsterdam: Elsevier)
Andersson, B.-G., Lazarian, A., & Vaillancourt, J. E. 2015, ARA&A, 53, 501
Armitage, P. J. 2015, arXiv:1509.06382
Bacciotti, F., Girart, J. M., Padovani, M., et al. 2018, ApJL, 865, L12
Beckwith, S. V. W., Sargent, A. I., Chini, R. S., & Guesten, R. 1990, AJ,
Birnstiel, T., Dullemond, C. P., Zhu, Z., et al. 2018, ApJL, 869, L45
Cox, E. G., Harris, R. J., Looney, L. W., et al. 2018, ApJ, 855, 92
Dent, W. R. F., Pinte, C., Cortes, P. C., et al. 2019, MNRAS, 482, L29
Dong, R., Hall, C., Rice, K., et al. 2015, ApJL, 812, L32
Dullemond, C. P., Juhasz, A., Pohl, A., et al. 2012, RADMC-3D: A multi-
  purpose radiative transfer tool, Astrophysics Source Code Library,
  ascl:1202.015
Durisen, R. H., Boss, A. P., Mayer, L., et al. 2007, Protostars and Planets V
  (Tucson, AZ: Univ. of Arizona Press), 607
Girart, J. M., Fernández-López, M., Li, Z.-Y., et al. 2018, ApJL, 856, L27
Harris, R. J., Cox, E. G., Looney, L. W., et al. 2018, ApJ, 861, 91
Hull, C. L. H., Yang, H., Li, Z.-Y., et al. 2018, ApJ, 860, 82
Kataoka, A., Muto, T., Momose, M., et al. 2015, ApJ, 809, 78
Kataoka, A., Tsukagoshi, T., Pohl, A., et al. 2017, ApJL, 844, L5
Konigl, A., & Pudritz, R. E. 2000, Protostars and Planets IV (Tucson, AZ:
  Univ. of Arizona Press), 759
Kwon, W., Stephens, I. W., Tobin, J. J., et al. 2019, ApJ, 879, 25
Lee, C.-F. 2010, ApJ, 725, 712
```

```
Lee, C.-F., Hwang, H.-C., & Li, Z.-Y. 2016, ApJ, 826, 213
Lee, C.-F., Jhan, K.-S., & Moraghan, A. 2023, ApJL, 951, L2
Lee, C.-F., Kwon, W., Jhan, K.-S., et al. 2019, ApJ, 879, 101
Lee, C.-F., Li, Z.-Y., Ching, T.-C., et al. 2018, ApJ, 854, 56
Lee, C.-F., Li, Z.-Y., & Turner, N. J. 2020, NatAs, 4, 142
Lee, C.-F., Li, Z.-Y., Yang, H., et al. 2021, ApJ, 910, 75
Lee, C.-F., Mao, Y.-Y., & Reipurth, B. 2009, ApJ, 694, 1395
Li, Z.-Y., Krasnopolsky, R., & Shang, H. 2013, ApJ, 774, 82
Lin, Z.-Y. D., Li, Z.-Y., Yang, H., et al. 2020, MNRAS, 493, 4868
Lin, Z.-Y. D., Lee, C.-F., Li, Z.-Y., et al. 2021, MNRAS, 501, 1316
Lin, Z.-Y. D., Li, Z.-Y., Stephens, I. W., et al. 2024, MNRAS, 528, 843
Machida, M. N., Inutsuka, S.-ichiro., & Matsumoto, T. 2008, ApJ, 676, 1088
Maury, A. J., Girart, J. M., Zhang, Q., et al. 2018, MNRAS, 477, 2760
Reipurth, B., Yu, K., Rodriguez, L. F., Heathcote, S., & Bally, J. 1999, A&A,
   352, L83
Sadavoy, S. I., Stephens, I. W., Myers, P. C., et al. 2019, ApJS, 245, 2
Shu, F. H., Najita, J. R., Shang, H., & Li, Z.-Y. 2000, Protostars and Planets IV
```

(Tucson, AZ: Univ. of Arizona Press), 789

```
Stephens, I. W., Yang, H., Li, Z.-Y., et al. 2017, ApJ, 851, 55
Stephens, I. W., Lin, Z.-Y. D., Fernández-López, M., et al. 2023, Natur, 623, 705
Takakuwa, S., Saigo, K., Kido, M., et al. 2024, ApJ, 964, 24
Tang, Y.-W., Dutrey, A., Koch, P. M., et al. 2023, ApJL, 947, L5
Tazaki, R., Lazarian, A., & Nomura, H. 2017, ApJ, 839, 56
Tazaki, R., Tanaka, H., Kataoka, A., et al. 2019, ApJ, 885, 52
Tobin, J. J., Sheehan, P. D., Megeath, S. T., et al. 2020, ApJ, 890, 130
Toomre, A. 1964, ApJ, 139, 1217
Turner, N. J., Fromang, S., Gammie, C., et al. 2014, Protostars and Planets VI (Tucson, AZ: Univ. of Arizona Press), 411
van't Hoff, M. L. R., Tobin, J. J., Li, Z.-Y., et al. 2023, ApJ, 951, 10
Yang, H., Fernández-López, M., Li, Z.-Y., et al. 2024, ApJ, 963, 134
Yang, H., Li, Z.-Y., Looney, L., & Stephens, I. 2016, MNRAS, 456, 2704
```

Yang, H., Li, Z.-Y., Looney, L. W., Girart, J. M., & Stephens, I. W. 2017, MNRAS, 472, 373